Optimizing Modal Traveling-Wave-Based Fault Location In Electrical Power Systems

Yang Lei[1], Fan Yang[1], Jinrui Tang[2*], Bo Ma[2], Guoqing Zhang[3], Yongjiang Han[3], Yu Shen[1], and Zhichun Yang[1]

[1] State Grid Hubei Electric Power Research Institute, 227 Xudong Road, 430077, Wuhan, China
[2] School of Automation, Wuhan University of Technology, 122 Luoshi Road, 430077, Wuhan, China
[3] Zhilian Xinneng Electric Power Technology Company, 6 Kejiyuan Road, 430223, Wuhan, China
[*] Corresponding author. E-mail: tangjinrui@hotmail.com

Received: Dec. 05, 2023; Accepted: Mar. 14, 2024

In power transmission networks, traditional double-ended traveling-wave-based fault-location methods have been widely utilized, demonstrating position errors of less than five hundred meters. However, when these traditional methods are directly applied to electrical distribution systems, the complex structures and parameters of distribution feeders necessitate the installation of numerous sensors to capture traveling waves. To minimize the total number of sensors required, it is advisable to employ both aerial-mode and zero-mode traveling waves for fault location, instead of relying solely on aerial-mode waves. In this paper, the distributed parameter-based line model is constructed and Karenbuaer transformation is used to achieve the mathematical model of modal traveling wave propagation speed, which is associated with various frequencies. And then the propagation speeds of zero-mode and aerial-mode fault-generated traveling waves are analyzed and compared with each other under overhead lines and underground cables in electrical distribution systems. Furthermore, the propagation speed is examined in main feeders and laterals with varying line radiuses and heights. The results indicate that zero-mode traveling waves can be utilized for fault location, but how to extract the real propagation speed under different fault distances would be the key factors to realize accurate modal traveling-wave-based fault location.

Keywords: Electrical distribution systems, fault location, traveling wave, propagation speed, line parameters.

http://dx.doi.org/10.6180/jase.202503_28(3).0008

1. Introduction

In today's world, customers demand high power supply reliability to enhance their quality of life and prevent disruptions in production. In electrical distribution systems, single-phase-to-ground and phase-to-phase faults are common occurrences, especially in low-altitude overhead lines located in wooded areas or along roadways [1]. The process of inspecting fault positions requires significant manpower and consumes a substantial amount of time [2]. Consequently, customers residing in the affected areas experience prolonged blackouts. Hence, precise identification of fault positions holds the utmost importance for electric utilities. Several automation devices have been implemented to capture fault-generated current or voltage signals, such as feeder remote terminal units and fault indicators [3]. Additionally, numerous fault location algorithms have been suggested by researchers to determine the fault section or position within electrical distribution systems, utilizing the sampled fault-generated signals [4]. These fault position location algorithms can be broadly categorized into three groups: power-frequency-components based algorithms [5–7], fault-generated transient-components based algo-

rithms [8–10], and traveling-wave based algorithms [11, 12].

Power-frequency-components based fault location algorithms involve calculating the impedance of the fault section from the measurement point to the fault point based on the selection of the faulty phase. The fault position is then determined by considering the calculated impedance of the fault section and the impedance per unit length. These algorithms are suitable for locating faults in transmission systems. However, in electrical distribution systems, the feeder topology is complex, and the presence of additional laterals can affect the impedance calculation [13, 14]. Moreover, these algorithms are not applicable for locating single-phase-to-ground faults in neutral noneffective grounded distribution systems (NGDSs) due to the fact that the weak fault current is primarily influenced by the capacitance to the ground of the conductors.

Fault-generated transient-components based fault location algorithms are primarily employed to identify the fault section in transmission or distribution power systems. These algorithms rely on analyzing the transient voltage and current signals, which are influenced by the series resistance, series inductance, and shunt capacitance situated on each side of the fault position. By comparing the differences between the transient signals detected upstream and downstream of the fault position, the fault section can be determined. However, due to the complex nature of transient signals, consisting of multiple frequency components, accurately pinpointing the fault position based on these time-varying signals poses a significant challenge.

Among various fault location algorithms, traveling-wave-based methods stand out for their high precision in fault localization. These methods have found applications in both transmission networks and distribution networks through the utilization of traveling-wave-based fault sensors [15–17]. In transmission network projects, two traveling-wave capture devices are installed at the starting and ending points of the transmission line, and the time difference between the recorded arrival of traveling waves is used to pinpoint the fault location. However, applying these conventional fault location algorithms directly to electrical distribution systems poses challenges. Distribution systems typically consist of multiple laterals connected to the main trunk, which itself comprises line sections with varying diameters. This leads to variations in traveling wave speed among different line sections and the occurrence of refraction and reflection at junction points. Consequently, the recorded time difference between the starting and ending points of the main trunk cannot be used to accurately locate the fault position.

Nowadays, artificial intelligence (AI) algorithms, which have been given many attentions by scholars, have also been applied in fault location in power systems. In literature [18, 19], the whole fault detection and isolation framework was proposed and discussed based on the natural switching behavior and disturbances in power systems. Based on these characteristics, Support Vector Regression (SVR), deep convolutional neural network (CNN) and other algorithms are introduced into the fault location to automatically detect the fault without gathering abundant detailed parameters of transmission lines or other components [20, 21]. The results show that AI-based fault location algorithms would become one powerful tool to improve the accuracy and efficiency in fault handling processes [22]. But these methods can only locate the fault section at the present stage, and it cannot locate the fault with the position errors of hundreds of meters.

Furthermore, the use of both aerial and zero-modal traveling waves during the location process can significantly reduce the total number of traveling wave sensors. However, it should be noted that the characteristics of zero-mode and aerial mode waves differ distinctly, particularly in the presence of overhead lines and underground cables. Hence, applying traditional fault location algorithms in distribution systems necessitates a comprehensive analysis of the propagation characteristics of modal traveling waves.

Since the propagation speed of the aerial-mode waves is stable and equals 3.0×10^8 m/s, only aerial-mode waves are used in traditional methods. However, when these traditional methods are directly applied to electrical distribution systems, the complex structures and parameters of distribution feeders necessitate the installation of numerous sensors to capture traveling waves, including the end of laterals, conjunction nodes, and the junctions of overhead lines and underground cables. In this paper, the arrival time difference of the fault-generated aerial-mode and zero-mode traveling waves is used to locate the fault. The wave sensors could be reduced significantly by simultaneous using modal traveling waves. But the traveling speed of zero-mode traveling waves has not been discussed in previous papers. Therefore, the distributed parameter-based line model is constructed and Karenbuaer transformation is used to achieve the mathematical model of modal traveling wave propagation speed, which is associated with various frequencies.

In order to address the challenges, we have conducted an in-depth analysis and comparison of fault-generated traveling waves in overhead lines and underground cables with varying parameters. This analysis takes into consideration the complex phenomena of refraction and reflection

that occur in wavefronts within electrical distribution systems. The objective is to gain insights into the behavior of these traveling waves under different conditions. Additionally, simulation results and recorded traveling waves obtained from field measurements are utilized to validate and enhance the performance of conventional traveling wave-based fault location algorithms. Through this process, we aim to reduce the number of required wave sensors significantly while ensuring accurate fault location in distribution systems.

2. Materials and methods

As illustrated in Fig. 1, when a fault arises on the distribution overhead feeder, traveling waves generated by the fault propagate in both directions along the three-phase conductors.

To analyze the modal traveling waves characteristics, Karenbuaer transformation matrix "S" is used to decouple the mutual effect among the three conductors by Eq. (1):

$$\begin{bmatrix} i_0(t) \\ i_1(t) \\ i_2(t) \end{bmatrix} = \mathbf{S}^{-1} \begin{bmatrix} i_a(t) \\ i_b(t) \\ i_c(t) \end{bmatrix} = \frac{1}{3} \begin{bmatrix} 1 & 1 & 1 \\ 1 & -1 & 0 \\ 1 & 0 & -1 \end{bmatrix} \begin{bmatrix} i_a(t) \\ i_b(t) \\ i_c(t) \end{bmatrix} \quad (1)$$

where $i_a(t), i_b(t)$, and $i_c(t)$ represent the instantaneous current samples of phases A, B, and C; $i_0(t), i_1(t)$, and $i_2(t)$ represent the zero-mode, aerial-mode 1 , and aerial-mode 2 current corresponding to the phase currents.

Through analysis and experiments, it has been demonstrated that as the frequency increases, the attenuation constant and velocity of zero-mode traveling wave experience a noticeable rise. Moreover, the frequency exerts a greater influence on the characteristics of zero-mode wavefronts compared to aerial-mode wavefronts.

Fig. 2 depicts a typical 10 kV distribution line, including its tower geometry and line parameters. When considering the frequency dependency of the line parameters and the distributed losses, accurate calculations of the series and shunt parameter matrix can be achieved through the analysis of the electromagnetic field distribution. This approach allows for a precise determination of the line's characteristics and behavior. In our work, we constructed the distribution line in PSCAD/EMTDC simulation software, incorporating the geometry parameters and DC resistance. Subsequently, we employed the Jmarti line model to acquire the frequency-related parameters. The effectiveness of the simulation was validated through field tests, confirming the accuracy and reliability of our findings.

Table 1 presents the partial series impedance magnitudes matrix, while Table 2 displays the shunt admittance magnitudes matrix obtained from the PSCAD/EMTDC simulations at various frequencies. The symbols Z(*i*,*i*) and Y(*i*,*i*) represent the self-impedance and self-admittance per-unit length of conductor *i*. The off-diagonal elements, Z((*i*,*j*) and Y(*i*,*j*), indicate the mutual impedance and admittance between the corresponding conductors *i* and *j*, respectively.

To determine the velocities of modal wavefronts in the distribution line depicted in Fig. 2,Eqs. (2) and (3) can be employed. The line parameters associated with various frequencies can be acquired through the utilization of PSCAD/EMTDC simulation software.

$$v_1(f) = 2\pi f / imag\left(\sqrt{\left(R_{1(f)} + j2\pi f L_{1(f)}\right)\left(G_{1(f)} + j2\pi f C_{1(f)}\right)}\right) \quad (2)$$

$$v_0(f) = 2\pi f / imag\left(\sqrt{\left(R_{0(f)} + j2\pi f L_{0(f)}\right)\left(G_{0(f)} + j2\pi f C_{0(f)}\right)}\right) \quad (3)$$

where *imag* represents the imaginary part of the complex number. Meanwhile, $R_{1(f)}, L_{1(f)}, G_{1(f)}$ and $C_{1(f)}$ refer to the series resistance, the series inductance, the shunt conductance and shunt capacitance per unit length, respectively of the aerial mode associated with the frequency f. Similarly, $R_{0(f)}, L_{0(f)}, G_{0(f)}$ and $C_{0(f)}$ represent the series resistance, series inductance, shunt conductance and shunt capacitance per unit length of the zero mode corresponding to the frequency f. $v_1(f)$ and $v_0(f)$ indicate the velocities of fault-generated traveling waves for the aerial mode and zero mode, respectively, at the frequency f.

The attenuation constants of modal wavefronts can also be calculated by using Eqs. (4) and (5)

$$\alpha_1(f) = real\left(\sqrt{\left(R_{1(f)} + j2\pi f L_{1(f)}\right)\left(G_{1(f)} + j2\pi f C_{1(f)}\right)}\right) \quad (4)$$

$$\alpha_0(f) = real\left(\sqrt{\left(R_{0(f)} + j2\pi f L_{0(f)}\right)\left(G_{0(f)} + j2\pi f C_{0(f)}\right)}\right) \quad (5)$$

where *real* represents the real part of the complex number, while $\alpha_1(f)$ and $\alpha_0(f)$ are aerial-mode and zero-mode attenuation constants corresponding to the frequency f, respectively Similarly, the Karenbuaer transformation matrix is used to obtain the modal parameters matrix, $\mathbf{D}_i$, based

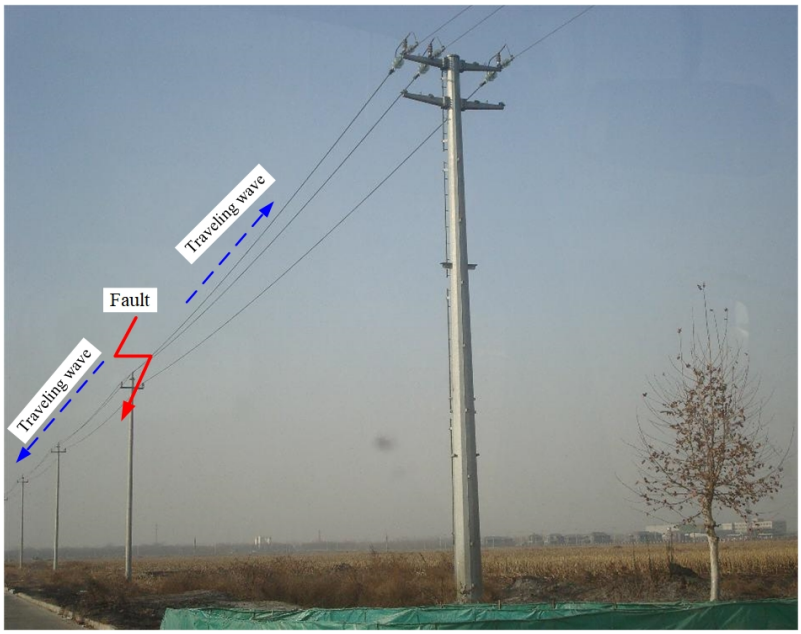

Fig. 1. One fault occurred on the distribution overhead feeder.

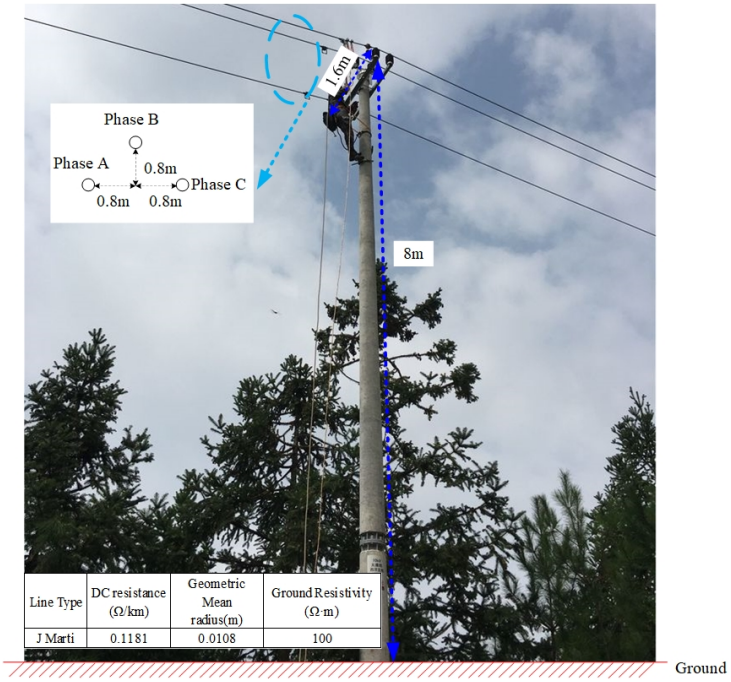

Fig. 2. Typical conductor data and tower geometry.

on the series impedance magnitudes matrix and shunt admittance magnitudes matrix.

$$\mathbf{D}_i = \mathbf{S}^{-1}\mathbf{ZYS} \tag{6}$$

Therefore, the modal parameters in Equations (2) and (3) can be derived as:

$$L_{1(f)} = imag\left[Z(i,i)_f\right] - imag\left[Z(i,j)_f\right] \tag{7}$$

$$R_{1(f)} = real\left[Z(i,i)_f\right] - real\left[Z(i,j)_f\right] \tag{8}$$

$$L_{0(f)} = imag\left[Z(i,i)_f\right] + 2imag\left[Z(i,j)_f\right] \tag{9}$$

Table 1. Partial series impedance magnitudes matrix corresponding to the distribution line shown in Fig. 1 (Ω/m).

F/Hz	Z(1,1)	Z(1,2)	Z(1,3)	Z(2,1)	Z(2,2)	Z(2,3)	Z(3,1)	Z(3,2)	Z(3,3)
0.5	1.19E − 04	5.66E − 06	5.66E − 06	5.66E − 06	1.19E − 04	5.66E − 06	5.66E − 06	5.66E − 06	1.19E − 04
51.9	7.80E − 04	4.38E − 04	4.38E − 04	4.38E − 04	7.80E − 04	4.38E − 04	4.38E − 04	4.38E − 04	7.80E − 04
4662	5.49E − 02	2.67E − 02	2.67E − 02	2.67E − 02	5.49E − 0	2.67E − 02	2.67E − 02	2.67E − 02	5.49E − 02
54928	0.574	0.245	0.245	0.245	0.574	0.245	0.245	0.245	0.574
559704	5.397	2.047	2.047	2.047	5.397	2.047	2.047	2.047	5.397

$$R_{0(f)} = real\left[Z(i,i)_f\right] + 2real\left[Z(i,j)_f\right] \tag{10}$$

$$C_{1(f)} = imag\left[Y(i,i)_f\right] - imag\left[Y(i,j)_f\right] \tag{11}$$

$$G_{1(f)} = real\left[Y(i,i)_f\right] - real\left[Y(i,j)_f\right] \tag{12}$$

$$C_{0(f)} = imag\left[Y(i,i)_f\right] + 2imag\left[Y(i,j)_f\right] \tag{13}$$

$$R_{0(f)} = real\left[Y(i,i)_f\right] + 2real\left[Y(i,j)_f\right] \tag{14}$$

By applying Eqs. (7) to (14), it is possible to derive the model parameters for fault-generated traveling waves. Subsequently, Eqs. (2) and (3) can be employed to determine the velocities of zero-mode and aerial-mode traveling waves. Additionally, Eqs. (4) and (5) can be utilized to calculate the attenuation constants of modal wavefronts.

3. Results and discussion

3.1. Propagation characteristics of traveling waves

The propagation properties of traveling waves encompass both the velocity at which modal traveling waves propagate and the attenuation constants. By utilizing Eqs. (2) to (5), the distribution feeder's characteristics depicted in Fig. 4 can be computed, resulting in their representation in Figs. 3 and 4. In Fig. 3, the frequency-dependent behavior of traveling waves is evident. Both the zero-mode speed and aerial-mode speed of traveling waves demonstrate an upward trend as the frequency increases. The zero-mode velocity ranges from 2.51×108 m/s to 2.89×108m/s, while the aerial-mode velocity ranges from 2.98×108 m/s to 3.00×108 m/s within the frequency range of 10 kHz to 1000 kHz. Notably, the amplitude of zero-mode velocity experiences a 15% increase, whereas the amplitude of aerial-mode velocity only shows a modest 0.7% increment. Consequently, when it comes to fault location in distribution power systems, relying on zero-mode traveling waves is not advisable due to their unstable propagation speed. Conversely, the propagation speed of aerial-mode traveling waves remains largely consistent, making them a more suitable choice for fault detection and localization.

Similarly, the attenuation constants of modal traveling waves can be determined and illustrated in Fig. 4. It is evident from the data that the attenuation constant of aerial-mode traveling waves is significantly lower than that of zero-mode traveling waves. Specifically, at frequencies below 1MHz, the attenuation constant of aerial-mode traveling waves is measured at 0.13×10^{-4}, whereas the attenuation constant of zero-mode traveling waves reaches

Table 2. Partial shunt admittance magnitudes matrix corresponding to the distribution line shown in Fig. 1 (S/m).

F/Hz	Y(1,1)	Y(1,2)	Y(1,3)	Y(2,1)	Y(2,2)	Y(2,3)	Y(3,1)	Y(3,2)	Y(3,3)
0.5	3.09E − 11	7.46E − 12	7.46E − 12	7.46E − 12	3.09E − 11	7.46E − 12	7.46E − 12	7.46E − 12	3.09E − 11
51.9	3.03E − 9	7.75E − 10	7.75E − 10	7.75E − 10	3.03E − 9	7.75E − 10	7.75E − 10	7.75E − 10	3.03E − 9
4662	2.72E − 7	6.96E − 8	6.96E − 8	6.96E − 8	2.72E − 7	6.96E − 8	6.96E − 8	6.96E − 8	2.72E − 7
54928	3.21E − 6	8.20E − 7	8.20E − 7	8.20E − 7	3.21E − 6	8.20E − 7	8.20E − 7	8.20E − 7	3.21E − 6
559704	3.27E − 5	8.35E − 6	8.35E − 6	8.35E − 6	3.27E − 5	8.35E − 6	8.35E − 6	8.35E − 6	3.27E − 5

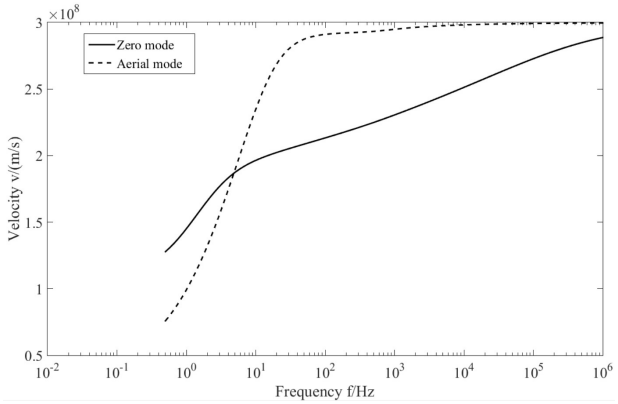

Fig. 3. Propagation velocities of modal traveling waves for distribution feeders in Fig. 1.

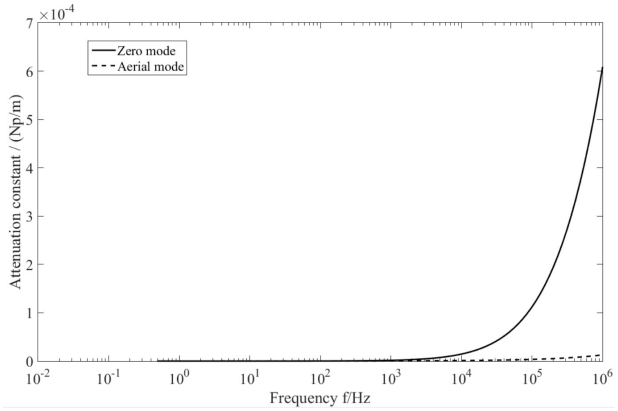

Fig. 4. Attention constant of modal traveling waves for distribution feeders in Fig. 1.

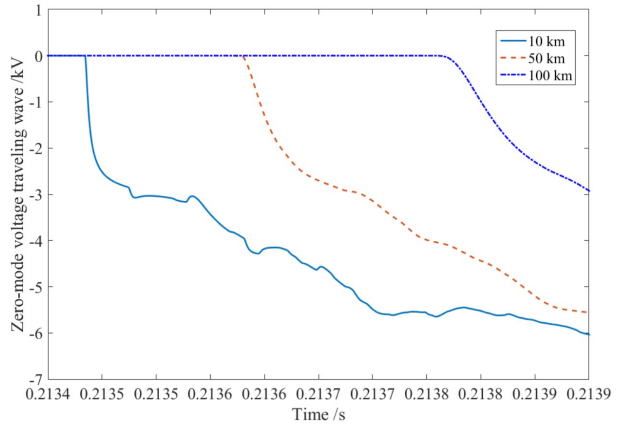

Fig. 5. Zero-mode traveling waves when fault distance changes for the feeders in Fig. 1.

6.1×10^{-4}. This discrepancy further highlights the favorable characteristics of aerial-mode traveling waves in terms of sustaining their amplitude over distance compared to

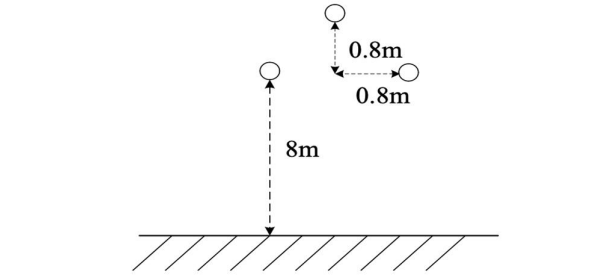

Line Type	DC resistance (Ω/km)	Geometric Mean radius(m)	Ground Resistivity (Ω·m)
J Marti	0.1181	0.0119	100

(a) One typical 10 kV distribution line

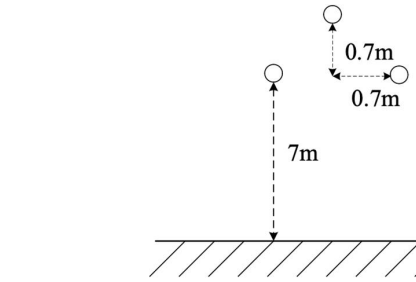

Line Type	DC resistance (Ω/km)	Geometric Mean radius(m)	Ground Resistivity (Ω·m)
J Marti	0.1181	0.0108	100

(b) Another typical 10 kV distribution line

Fig. 6. Typical conductor data and tower geometry for 10 kV distribution lines.

Table 3. Partial shunt admittance magnitudes matrix corresponding to the distribution line shown in Fig. 1 (S/m).

Geometr ic mean radius	Ground resistivity	Height of lowest	Spacing between	Propagation speed /(m/s)	
				zero-mode	aerial-mode
$(\Omega \cdot \mathrm{m})$	conductors	conductors	waves under 1	waves under 1 MHz	MHz
0.0108	100	8	0.8	2.89×10^8 m/s	3.00×10^8 m/s
0.0119	100	8	0.8	2.89×10^8 m/s	3.00×10^8 m/s
0.0108	100	7	0.7	2.87×10^8 m/s	3.00×10^8 m/s
0.0108	200	8	0.8	2.85×10^8 m/s	3.00×10^8 m/s

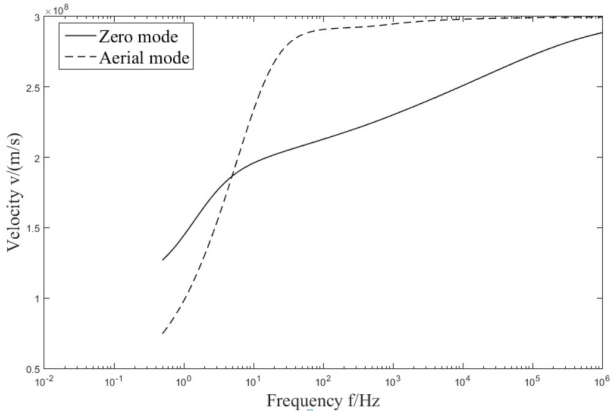

Fig. 7. Propagation velocities of modal traveling waves for distribution feeders in Fig. 6a.

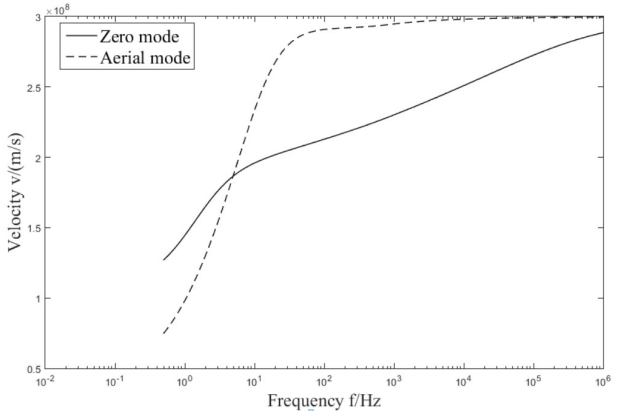

Fig. 8. Propagation velocities of modal traveling waves for distribution feeders in Fig. 6b.

zero-mode traveling waves. The analysis of the attenuation constants reveals a significant attenuation of zero-mode wavefronts compared to aerial-mode wavefronts. This finding is further supported by the simulation results displayed in Fig. 5, which depict the wavefront behavior at different propagation distances. As a result of its substantial attenuation, detecting the arrival time of zero-mode wavefronts becomes challenging due to its weakened signal strength.

3.2. 10 kV distribution overhead lines

In Section 3, the propagation characteristics of modal traveling waves were analyzed for the distribution feeder depicted in Fig. 2. However, it is important to note that in practical field scenarios, the distribution feeder typically comprises multiple line sections, each with its unique set of parameters. These parameters may include the geometric mean radius and the ground resistivity, among others.

The same analysis procedure is carried out for different

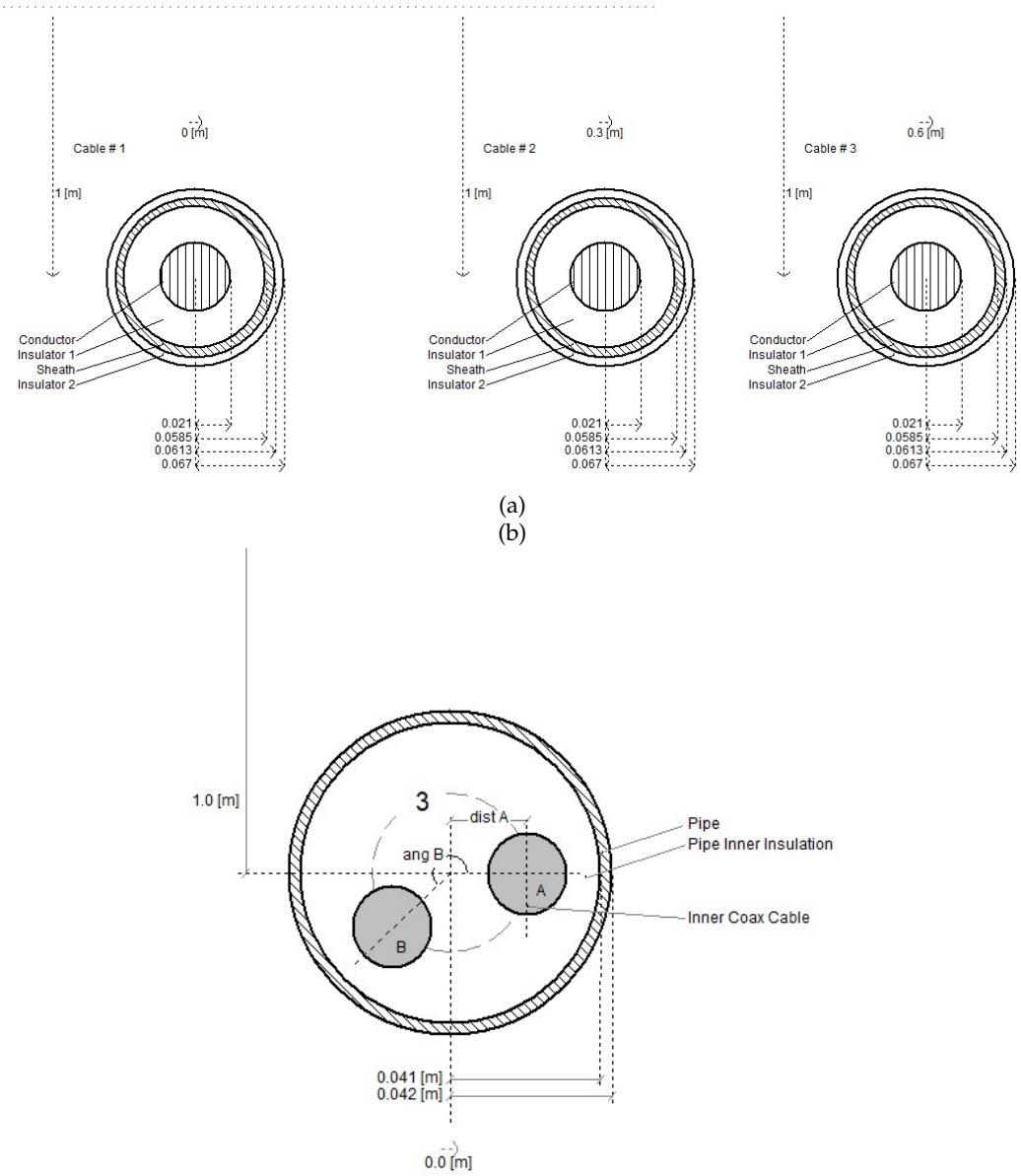

Fig. 9. Typical distribution of underground cables in this paper. (a) The typical coaxial cables with three conductors; (b) The typical pipe-type cables with three numbers of inner cables.

distribution lines with different parameters. The propagation speeds for the distribution feeder shown in Fig. 6(a) and Fig. 6 are presented in Figs. 7 and 8, respectively. A summary of the comparison results can be found in Table 3.

Table 3 indicates that the propagation speed of zero-mode waves exhibits variation when different parameters are applied to distribution lines. The variability in zero-mode speed is approximately 0.04×10^8 m/s, which can result in significant location errors within distribution power systems. Conversely, the variation in aerial-mode speed is approximately 0.001×10^8 m/s. Consequently, when utilizing aerial-mode traveling waves to identify fault locations, it is reasonable to assume a uniform propagation speed of 3.00×10^8 m/s across different line sections within a given distribution feeder. This assumption helps mitigate the impact of speed variations on fault location accuracy.

3.3. 10 kV distribution cable lines

In electrical power distribution networks, underground cables prevail as a preferred choice in urban districts to enforce immunity from environmental factors and ensure power supply reliability. The per-unit self inductance of underground cables is smaller than that of overhead lines,

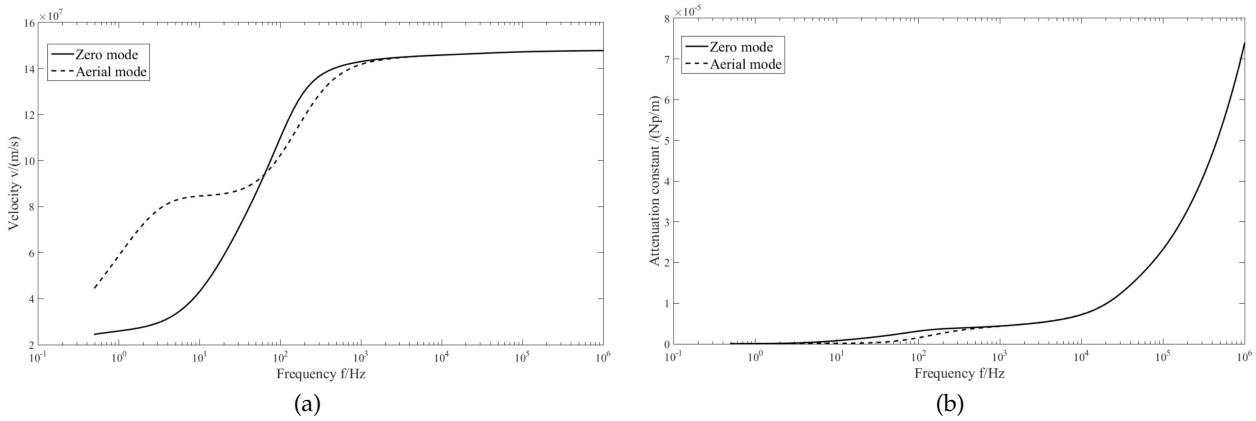

(a) (b)

Fig. 10. Propagation characteristics of modal traveling waves for cables shown in Fig. 9(a). (a) Propagation velocities of modal traveling waves; (b) Attention constant of modal traveling waves.

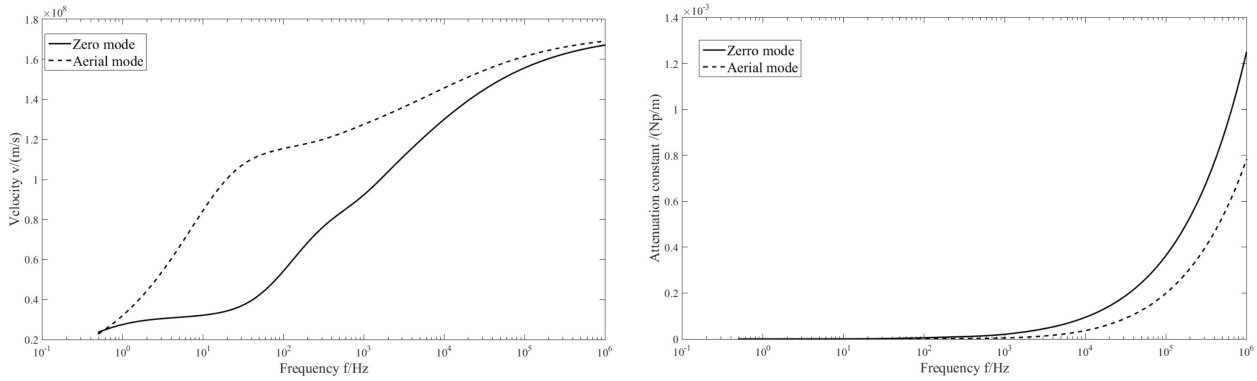

(a) (b)

Fig. 11. Propagation characteristics of modal traveling waves for cables shown in Fig. 9(b). (a) Propagation velocities of modal traveling waves; (b) Attention constant of modal traveling waves.

while the per-unit self capacitance of underground cables is much bigger than that of overhead lines.

Since there are many types and structures for underground cables, the coaxial cables with three conductors, and the pipe-type cables with three numbers of inner cables are considered in this work. These two types of cables are shown in Fig. 9.

Similar analysis has been carried out to obtain the propagation speeds and attenuation constants for underground cables with typical parameters. The analysis results for coaxial cables shown in Fig. 9(a) are presented in Fig. 10, while analysis results for pipe-type cables shown in Fig. 9(b) are illustrated in Fig. 11.

In Fig. 9(a), the analysis of coaxial cables reveals that the presence of insulators between each conductor mitigates the impact of mutual inductance and capacitance among the three-phase cables on the propagation characteristics of modal traveling waves. The propagation velocities and attenuation constants of modal traveling waves for coaxial cables, as shown in Fig. 9(a), are presented in Fig. 10(a) and Fig. 10(b), respectively. When the frequency exceeds 100 Hz, the propagation velocities and attenuation constants of aerial modal traveling waves become almost identical to those of zero nodal traveling waves across different frequencies. Notably, for the coaxial cables, whether in the aerial mode or zero mode, the propagation velocity ranges from 1.473×10^8 m/s to 1.478×10^8 m/s when the frequency varies from 100kHz to 1MHz.

In China, pipe-type cables with three inner cables are widely used for 10kV medium-voltage applications, and a representative pipe-type cable is illustrated in Fig. 9(b). In the case of pipe-type cables, the coupling among the three-phase conductors cannot be neglected in the analysis of traveling wave propagation. As demonstrated in Fig. 11(a) and Fig. 11(b), the velocity of aerial modal traveling waves ranges from 1.621×10^8 m/s to 1.691×10^8 m/s,

while the velocity of zero mode traveling waves varies from 1.566×10^8 m/s to 1.671×10^8 m/s, as the frequency changes from 100kHz to 1MHz. These findings emphasize the influence of coupling among the conductors and highlight the frequency-dependent variations in the velocities of aerial modal and zero-mode traveling waves in pipe-type cables. Based on the analysis results mentioned above, it can be concluded that the velocities of traveling waves exhibit greater volatility in pipe-type cables compared to coaxial cables. Additionally, the velocities of traveling waves in underground cables are significantly lower than those observed in overhead lines. These observations highlight the distinctive characteristics and behavior of traveling waves in underground cable systems, emphasizing the need for careful consideration and analysis when designing and evaluating their performance in power distribution networks.

3.4. 110 kV transmission lines

110 kV transmission lines find extensive utilization in electrical distribution systems to supply electricity to large-scale commercial complexes or industrial parks. Fig. 12 illustrates various 110 kV distribution lines with diverse parameters, ranging from different conductors to tower geometries (Fig. 12a to Fig. 12f). The propagation speeds of traveling waves for these lines have been determined and consolidated, as presented in Table 4.

Analysis of Table 4 reveals that the propagation speed of zero-mode waves exhibits variability depending on the parameters of 110kV distribution lines. This variation in zero-mode speed amounts to approximately 0.038×10^8 m/s, potentially resulting in significant location errors. Conversely, the aerial-mode speed variation is approximately 0.003×10^8 m/s. Consequently, when employing aerial-mode traveling waves to determine the location of faults in 110kV transmission lines, it is reasonable to consider the propagation speed as consistent across different line sections within a given 110kV distribution line. The modal velocities of traveling waves for the 110kV transmission lines depicted in Fig. 8a have been calculated in a similar manner and are presented in Fig. 13.

In the case of 110kV transmission lines, the zero-mode velocity ranges from 2.66×10^8 m/s to 2.93×10^8 m/s, while the aerial-mode velocity ranges from 2.98×10^8 m/s to 2.99×10^8 m/s. Notably, both velocities exhibit an increasing trend as the frequency varies from 10kHz to 1000kHz. The amplitude of the zero-mode velocity experiences a 10% increase, whereas the amplitude of the aerial-mode velocity only sees a marginal 0.3% increase. Based on the analysis of Fig. 12c and Fig. 12d, it has been

Table 4. Propagation speeds of different 110 kV distribution lines.

Tower geometries	Geometric mean radius /m	Height of lowest conductors /m	Spacing between conductors /m	Number of overhead ground wires	Propagation speed /(m/s)	
					Zero-mode waves under 1 MHz	Aerial-mode waves under 1 MHz
Fig. 12 a	0.0138	15	4	1	2.928×10^8 m/s	2.993×10^8 m/s
Fig. 12b	0.0138	24	4	1	2.965×10^8 m/s	2.996×10^8 m/s
Fig. 12 c	0.0138	24	4 and 7	1	2.960×10^8 m/s	2.996×10^8 m/s
Fig. 12 d	0.0138	24	4 and 7	2	2.966×10^8 m/s	2.996×10^8 m/s
Fig. 12 e	0.0125	15	4	1	2.929×10^8 m/s	2.993×10^8 m/s
Fig. 12 f	0.0125	24	4	1	2.966×10^8 m/s	2.996×10^8 m/s

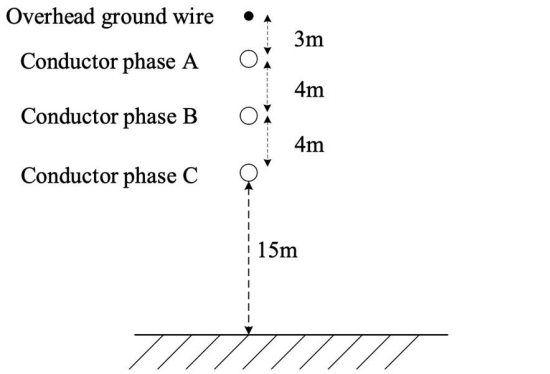

Line Type	DC resistance (Ω/km)	Geometric Mean radius(m)	Ground Resistivity (Ω·m)
J Marti	0.0723	0.0138	100

(a) The first-type 110 kV distribution line

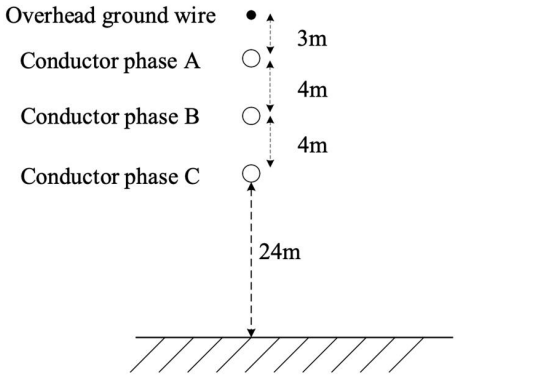

Line Type	DC resistance (Ω/km)	Geometric Mean radius(m)	Ground Resistivity (Ω·m)
J Marti	0.0723	0.0138	100

(b) The second-type 110 kV line

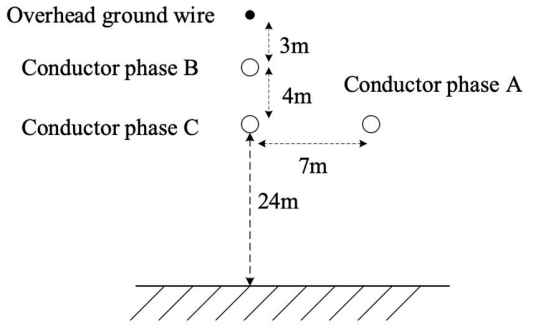

Line Type	DC resistance (Ω/km)	Geometric Mean radius(m)	Ground Resistivity (Ω·m)
J Marti	0.0723	0.0138	100

(c) The third-type 110 kV line

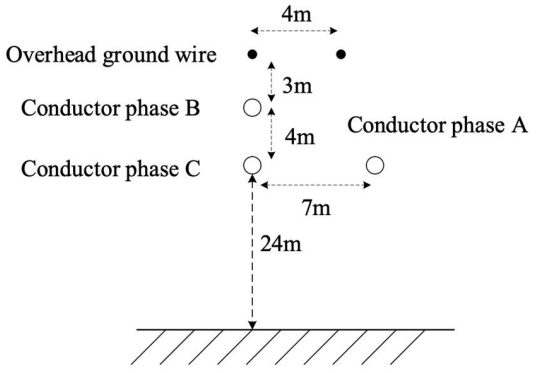

Line Type	DC resistance (Ω/km)	Geometric Mean radius(m)	Ground Resistivity (Ω·m)
J Marti	0.0723	0.0138	100

(d) The fourth 110 kV line

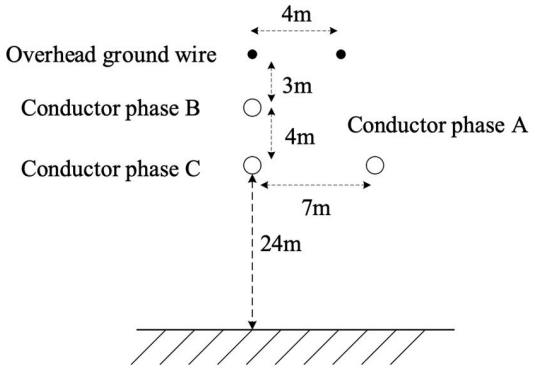

Line Type	DC resistance (Ω/km)	Geometric Mean radius(m)	Ground Resistivity (Ω·m)
J Marti	0.0723	0.0138	100

(e) The fifth-type 110kV line

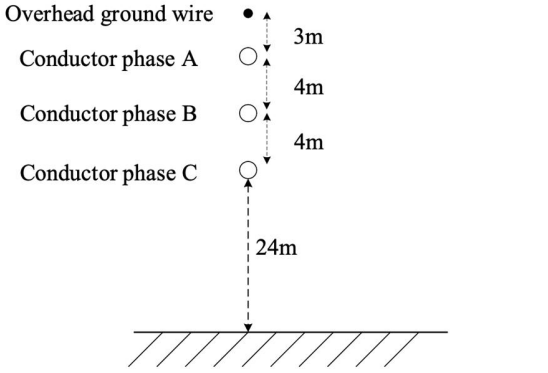

Line Type	DC resistance (Ω/km)	Geometric Mean radius(m)	Ground Resistivity (Ω·m)
J Marti	0.0946	0.0125	100

(f) The sixth-type 110kV line

Fig. 12. Typical 110 kV transmission lines with different conductors and tower geometries.

determined that the presence of protective conductors exclusively impacts the zero-mode traveling waves. Further investigation reveals that by altering the number of overhead ground wires from 1 to 2 , the zero-mode speed expe-

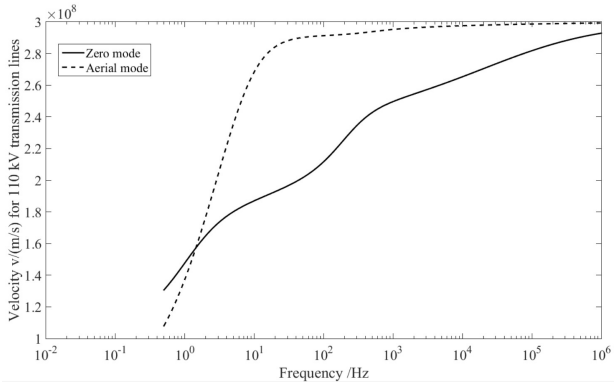

Fig. 13. Propagation velocities of modal traveling waves for 110 kV line in Fig. 12a

riences changes from 2.960×10^8 m/s to 2.966×10^8 m/s at 1000kHz, and from 2.762×10^8 m/s to 2.806×10^8 m/s at 10kHz. However, the aerial-mode speed remains unaffected by the presence of protective conductors.

4. Conclusions

This paper analyzes and compares the propagation speed and attenuation constants of fault-generated modal traveling waves under different distribution feeders with varying parameters. The findings indicate that the speed volatility of zero-mode traveling waves is significantly greater than that of aerial-mode traveling waves. In electrical distribution systems, when power utilities have the financial resources to invest in traditional aerial-mode traveling wave sensors installed at various lateral terminal points, utilizing the arriving time differences of multiple aerial-mode waves becomes a favorable approach for fault location. Else, an alternative approach is to employ both aerial-mode and zero-mode traveling waves for fault location. The initial arrival time of aerial wavefronts differs from that of zero-mode wavefronts due to the disparity in propagation speed. This approach allows for the use of fewer sensors, leading to a significant reduction in investment costs.

Notably, when the frequency ranges from 10kHz to 1000kHz, the speed volatility of zero-mode traveling waves on 10kV distribution overhead lines ranges from 2.51×10^8 m/s to 2.89×10^8 m/s, while on 110kV transmission overhead lines, it ranges from 2.66×10^8 m/s to 2.93×10^8 m/s. Additionally, the propagation speed of aerial modal traveling waves in underground cables is considerably lower than that in overhead lines, varying from 1.621×10^8 m/s to 1.691×10^8 m/s for typical pipe-type cables with three inner cables. In the future, the identification of zero-mode propagation speed through intelligent algorithms can enhance fault location accuracy.

Acknowledgments

This work was supported by State Grid Hubei Electric Power Company under Grant No.B3153221001K.

Data availability statement

The data used to support the findings of this study are included within the article.

Conflicts of interest

The authors declare that they have no competing interest.

References

[1] L. K. Mortensen, H. R. Shaker, and C. T. Veje, (2022) *"Relative fault vulnerability prediction for energy distribution networks"* **Applied Energy *322***: 119449. DOI: 10.1016/j.apenergy.2022.119449.

[2] C. Yang, S. Lin, and M. Guo, (2022) *"Multi-Frequency bands based Pole-to-Ground fault detection method for MMC-Based radial DC distribution systems"* **International Journal of Electrical Power Energy Systems *141***: 108250. DOI: 10.1016/j.ijepes.2022.108250.

[3] A. Shammah, A. A. El-Ela, and A. M. Azmy, (2012) *"Optimal location of remote terminal units in distribution systems using genetic algorithm"* **Electric Power Systems Research *89***: 165–170. DOI: 10.1016/j.epsr.2012.03.007.

[4] P. Stefanidou-Voziki, N. Sapountzoglou, B. Raison, and J. Dominguez-Garcia, (2022) *"A review of fault location and classification methods in distribution grids"* **Electric Power Systems Research *209***: 108031. DOI: 10.1016/j.epsr.2022.108031.

[5] L. Zang, G. Zou, C. Zhou, M. Zheng, and T. Du, (2022) *"Ad-axis based current differential protection scheme for an active distribution network"* **Protection and Control of Modern Power Systems *7***(2): 1–11. DOI: 10.1186/s41601-022-00243-0.

[6] E. Gord, R. Dashti, M. Najafi, and H. R. Shaker, (2019) *"Real fault section estimation in electrical distribution networks based on the fault frequency component analysis"* **Energies *12***(6): 1145. DOI: 10.3390/en12061145.

[7] R. Rubeena, M. R. Dadash Zadeh, and T. P. S. Bains, (2014) *"An Accurate Offline Phasor Estimation for Fault Location in Series-Compensated Lines"* **IEEE Transactions on Power Delivery *29***(2): 876–883. DOI: 10.1109/TPWRD.2013.2283454.

[8] R. Benato, G. Rinzo, and M. Poli, (2019) *"Overcoming the limits of the charge transient fault location algorithm by the artificial neural network"* **Energies *12***(4): 722. DOI: 10.3390/en12040722.

[9] S.-y. He, A. Cozza, and Y.-z. Xie, (2020) *"On the Spatial Resolution of Fault-Location Techniques Based on Full-Fault Transients"* **IEEE Transactions on Power Delivery *35***(3): 1527–1540. DOI: 10.1109/TPWRD.2019.2949914.

[10] K. Jia, T. Feng, Q. Zhao, C. Wang, and T. Bi, (2020) *"High Frequency Transient Sparse Measurement-Based Fault Location for Complex DC Distribution Networks"* **IEEE Transactions on Smart Grid *11***(1): 312–322. DOI: 10.1109/TSG.2019.2921301.

[11] L. Xie, L. Luo, J. Ma, Y. Li, M. Zhang, X. Zeng, and Y. Cao, (2022) *"A novel fault location method for hybrid lines based on traveling wave"* **International Journal of Electrical Power & Energy Systems *141***: 108102. DOI: 10.1016/j.ijepes.2022.108102.

[12] J. Ding, L. Li, Y. Zheng, C. Zhao, H. Chen, and X. Wang, (2017) *"Distributed travelling-wave-based fault location without time synchronisation and wave velocity error"* **IET Generation, Transmission & Distribution *11***(8): 2085–2093. DOI: 10.1049/iet-gtd.2016.1778.

[13] C. Orozco-Henao, A. Suman Bretas, J. Marín-Quintero, A. Herrera-Orozco, J. D. Pulgarín-Rivera, and J. C. Velez, (2018) *"Adaptive impedance-based fault location algorithm for active distribution networks"* **Applied sciences *8***(9): 1563. DOI: 10.3390/app8091563.

[14] M. Daisy and R. Dashti, (2016) *"Single phase fault location in electrical distribution feeder using hybrid method"* **Energy *103***: 356–368. DOI: 10.1016/j.energy.2016.02.097.

[15] X. Tian and H. Shu, (2021) *"A new method of single terminal traveling wave location based on characteristic of superposition of forward traveling wave and backward traveling wave"* **International Journal of Electrical Power Energy Systems *133***: 107072. DOI: 10.1016/j.ijepes.2021.107072.

[16] W. Chen, D. Wang, D. Cheng, F. Qiao, X. Liu, and M. Hou, (2022) *"Novel travelling wave fault location principle based on frequency modification algorithm"* **International Journal of Electrical Power Energy Systems *141***: 108155. DOI: 10.1016/j.ijepes.2022.108155.

[17] V. Gonzalez-Sanchez, V. Torres-García, and D. Guillen, (2021) *"Fault location on transmission lines based on travelling waves using correlation and MODWT"* **Electric Power Systems Research *197***: 107308. DOI: 10.1016/j.epsr.2021.107308.

[18] A. Tanwani, A. D. Dominguez-Garcia, and D. Liberzon, (2011) *"An Inversion-Based Approach to Fault Detection and Isolation in Switching Electrical Networks"* **IEEE Transactions on Control Systems Technology *19***(5): 1059–1074. DOI: 10.1109/TCST.2010.2067214.

[19] F. G. Y. Souhe, A. T. Boum, P. Ele, C. F. Mbey, V. J. F. Kakeu, et al., (2022) *"Fault detection, classification and location in power distribution smart grid using smart meters data"* **Journal of Applied Science and Engineering *26***(1): 23–34. DOI: 10.6180/jase.202301_26(1).0003.

[20] J. B. Thomas, S. G. Chaudhari, S. K. V., and N. K. Verma, (2023) *"CNN-Based Transformer Model for Fault Detection in Power System Networks"* **IEEE Transactions on Instrumentation and Measurement *72***: 1–10. DOI: 10.1109/TIM.2023.3238059.

[21] W. Elmasry and M. Wadi, (2022) *"Edla-efds: A novel ensemble deep learning approach for electrical fault detection systems"* **Electric Power Systems Research *207***: 107834. DOI: 10.1016/j.epsr.2022.107834.

[22] F. M. Shakiba, S. M. Azizi, M. Zhou, and A. Abusorrah, (2023) *"Application of machine learning methods in fault detection and classification of power transmission lines: a survey"* **Artificial Intelligence Review *56***(7): 5799–5836. DOI: 10.1007/s10462-022-10296-0.